

# Bioresorbable Primary Battery Anodes Built on Core–Double-Shell Zinc Microparticle Networks

Yutao Dong, Jun Li, Fan Yang, Yizhan Wang, Ziyi Zhang, Jingyu Wang, Yin Long, and Xudong Wang\*



Cite This: *ACS Appl. Mater. Interfaces* 2021, 13, 14275–14282



Read Online

ACCESS |



Metrics & More



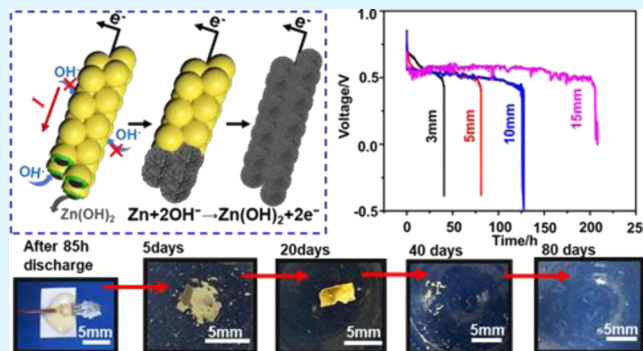
Article Recommendations



Supporting Information

**ABSTRACT:** Bioresorbable implantable electronics require power sources that are also bioresorbable with controllable electrical output and lifetime. In this paper, we report a bioresorbable zinc primary battery anode filament based on a zinc microparticle (MP) network coated with chitosan and  $\text{Al}_2\text{O}_3$  double shells. When discharged in 0.9% NaCl saline, a Zn MP filament with a  $0.17 \times 2 \text{ mm}^2$  cross-sectional area exhibited a stable voltage output of 0.55 V at a current of 0.01 mA. Covered by chitosan and  $\text{Al}_2\text{O}_3$  double shells, the zinc MP filament exhibited a directional dissolution behavior with a tunable lifetime approximately linear to its length. A stable 200 h discharging time was achieved with a 15 mm Zn MP filament. The maximum output power was found to be  $12 \mu\text{W}$  at 0.03 mA for one filament. The linearity relationship between the current output and the filament cross-sectional area suggested a facile strategy to raise the power output at constant discharging voltage. The filaments could also be connected in series and in parallel to boost its overall voltage and current output, demonstrating their excellent integration capability. This work presents a promising pathway toward bioresorbable transient batteries with controllable lifetime and power output, demonstrating a great potential for powering transient implantable biomedical devices.

**KEYWORDS:** bioresorbable battery anode, Zn microparticles, core–double-shell network, directional discharge, transient electronics



## 1. INTRODUCTION

Bioresorbable electronics are a type of electronic devices that decompose in the physiological environment after a designed period of stable function, and the corresponding byproducts are resorbed and vanish.<sup>1</sup> They are gaining increasing research interest in state-of-the-art biomedical implants for pre-diagnosis, monitoring, and treatment of diseases, drug delivery, and tissue regeneration, which only require the function for a certain period of time.<sup>2,3</sup> Introducing complete biodegradability can eliminate additional surgery procedures to remove the implants and minimize relevant medical complications and cost. To date, various bioresorbable electronics based on Si, metal, alloy, and organics have been reported.<sup>4–9</sup> However, their practical applications are largely limited by the slow evolution of power supplies that also need to be bioresorbable with a designed lifetime. Bioresorbable piezoelectric energy harvesters<sup>10,11</sup> and supercapacitors have been developed as potential transient power sources, but they are still confronted with either low energy density or discontinuous power output.<sup>12–14</sup> Bioresorbable primary batteries are a promising power source for transient medical implants because of their relatively higher energy density and continuous power output. They are typically composed of bioresorbable materials that

degrade into non-toxic contents in the physiological environment during and/or after discharge.

In bioresorbable batteries, bioresorbable chemicals such as melanin, dissolvable metals and alloys,<sup>15</sup> and metal oxide are typically implemented in the electrode design.<sup>16</sup> The electrolyte normally uses a biocompatible liquid, such as NaCl saline and phosphate-buffered saline (PBS) or polymer electrolytes with ionic liquid.<sup>17</sup> State-of-the-art bioresorbable batteries are built upon Mg or Zn metal-based galvanic cells due to their good biosafety and electrochemical activity. Fully bioresorbable Mg–Mo (W, Fe, and  $\text{MoO}_3$ ) primary battery systems in the PBS electrolyte demonstrated up to  $\sim 1.6 \text{ V}$  output voltage with a current density at the level of tens of  $\mu\text{A cm}^{-2}$ , which were feasible to power small electronics.<sup>16,18,19</sup> Besides, from Mg–Fe batteries, both 0.9% NaCl and  $1\times$  PBS electrolytes yielded similar discharge lifetime, average voltage output, and specific capacity, suggesting minimal differences from these

**Received:** January 11, 2021

**Accepted:** March 9, 2021

**Published:** March 17, 2021



two commonly used biocompatible electrolytes.<sup>19</sup> Other Mg-based systems included Mg–air and Mg alloy (AZ31B)–air cells that yielded  $\sim 0.95$  V at  $10 \mu\text{A cm}^{-2}$ .<sup>17</sup> However, Mg-based primary batteries always involve hydrogen gas generation reactions, which is risky in the human body. Due to the very high chemical activity, current Mg-based bioresorbable batteries all exhibited fluctuating voltage output and rapid output drops without a controllable lifetime, which cannot meet the requirements of an implantable power supply.<sup>16,18–20</sup> Additionally, the fast degradation rate could induce localized release of concentrated hydroxyl ions, leading to inflammation or other harmful effects.<sup>21,22</sup> Compared to Mg, Zn metal has a moderate degradation rate, which can circumvent undesirable local pH increases and minimize gaseous hydrogen evolution.<sup>23</sup> An ingestible Zn–Cu cell was reported in the gastrointestinal (GI) tract with an average of 6.1 day lifetime, providing a relatively stable output, but it required an acidic environment.<sup>24</sup> In bioresorbable metal-based galvanic cell systems, although both the anode and cathode are needed, it is the metal anode that dissolves in the electrolyte and primarily determines battery lifetime and power output. Nevertheless, almost all current anode models were built on bulky foils or plates, where their degradation occurred naturally on the metal surface. Therefore, there was no control over the degradation rate, direction, and sequence, and thus, all showed poor controllability on the battery output and lifetime. Here, we report a bioresorbable zinc primary battery anode filament built on Zn microparticles (MPs) coated with biocompatible chitosan and  $\text{Al}_2\text{O}_3$  nano-films. This anode filament exhibited a well-controlled dissolution direction due to the mesoscale MP assembly and the conductive and protective coatings. A single filament could deliver a stable voltage of 0.55 V at 0.01 mA, where the current and voltage output could be simply designed by integration of the battery filaments in parallel or in series, respectively. The operational time could be directly adjusted by the length of the filament. This bioresorbable primary battery showed a full level of control of output and lifetime, providing a promising solution to *in vivo* powering transient bioelectronics.

## 2. RESULTS AND DISCUSSION

The processing of a degradable battery anode is schematically shown in Figure 1a (the fabrication details are given in the Experimental Section). Acetic acid treatment was used to clean up oxides from the Zn MP surfaces to achieve better contacts in between after sintering. Chitosan (CS) was used as a binder to enhance the flexibility and biocompatibility of the Zn MP network. To control the dissolution of the zinc–chitosan composite electrode, a thin layer of  $\text{Al}_2\text{O}_3$  was introduced by atomic layer deposition (ALD) to the composite surface to adjust water permeability to Zn MPs. The final electrode configuration had a  $\text{Zn@CS@Al}_2\text{O}_3$  core–double-shell structure, as shown in Figure 1a. The composite electrode material could be casted on a flat substrate with arbitrary patterns to achieve rational control of the battery lifetime and electrical output. Figure 1b shows a simple filament geometry used in the performance test. Scanning electron microscopy (SEM) images showed the uniform three-dimensional network structure of an as-prepared  $\text{Zn@CS@Al}_2\text{O}_3$  filament electrode (Figure 1c). Zn MPs within the size range of 4–10  $\mu\text{m}$  were infused together, forming a porous network. The interconnected microscale pores allowed chitosan to migrate through and fully cover all Zn MP surfaces as the first shell layer. A

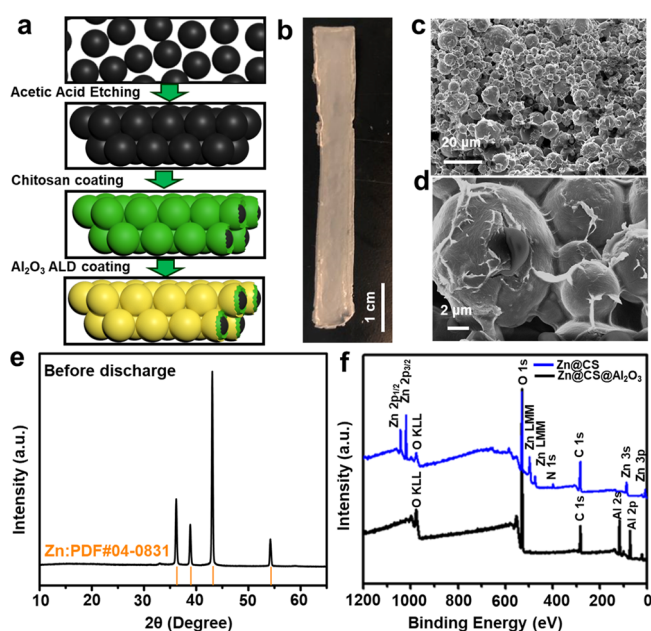


**Figure 1.** Processing and structural characterization of  $\text{Zn@CS@Al}_2\text{O}_3$  electrodes. (a) Schematic diagram showing the fabrication procedure of the  $\text{Zn@CS@Al}_2\text{O}_3$  core–double-shell structure. (b) Optical image of an as-prepared  $\text{Zn@CS@Al}_2\text{O}_3$  electrode with a dimension of  $6 \text{ cm} \times 0.7 \text{ cm} \times 0.17 \text{ mm}$ . (c) SEM image of an as-prepared  $\text{Zn@CS@Al}_2\text{O}_3$  network. (d) High-resolution SEM image showing tight connection between adjacent Zn MPs by double shells. (e) X-ray diffraction patterns of a  $\text{Zn@CS@Al}_2\text{O}_3$  structure before discharge. (f) XPS survey spectra of the  $\text{Zn@CS}$  composite before and after  $\text{Al}_2\text{O}_3$  coating.

higher magnification image further revealed that the chitosan binder was tightly wrapped around the Zn MPs, forming a continuous organic framework by  $-\text{NH}_2$  group chelation.<sup>25</sup> Such a microporous structure remained stable after 20 nm  $\text{Al}_2\text{O}_3$  coating was introduced (Figures 1d and S1). X-ray diffraction (XRD) spectra only showed strong Zn peaks (PDF#04-0831) and no ZnO peaks were detected (Figure 1e), confirming that the acetic acid treatment was successful in removing the surface passivation oxide layer, and the metallic Zn compound was well preserved during sintering and chitosan and ALD coating. In addition, no other peaks were observed from the XRD spectra either, suggesting that both chitosan and ALD-grown  $\text{Al}_2\text{O}_3$  were amorphous. X-ray photoelectron spectroscopy (XPS) was further performed for elemental analysis. In the XPS survey spectrum of chitosan-coated Zn MPs (upper curve in Figure 1f), both Zn and N 1s (139.1 eV, attributing to chitosan) signals could be clearly identified. After ALD  $\text{Al}_2\text{O}_3$  coating, the XPS spectrum (lower curve in Figure 1f) showed strong Al 2s (119.58 eV) and 2p (74.58 eV) peaks (attributing to alumina). Meanwhile, N 1s and Zn 2p peaks disappeared after ALD coating, indicating a conformal and uniform coating of the ALD  $\text{Al}_2\text{O}_3$  film on all exposed surfaces. The C 1s peak was attributed to surface contamination, which was usually detected in XPS. Energy-dispersive X-ray spectroscopy (EDS) mapping of  $\text{Zn@CS@Al}_2\text{O}_3$  (Figure S2) further showed that Al mapping overlapped well with C and Zn mapping, attributed to the CS layer and Zn MPs, respectively, confirming the uniform and complete coverage of  $\text{Al}_2\text{O}_3$  over entire irregular  $\text{Zn@CS}$  surfaces.

The  $\text{Zn@CS@Al}_2\text{O}_3$  core–double-shell structure was designed as the anode of a degradable Zn primary battery

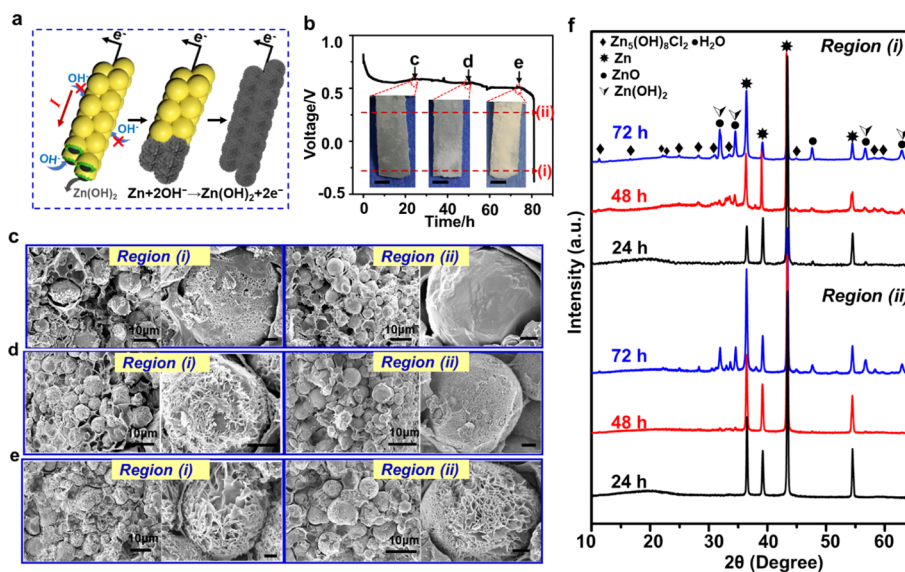


**Figure 2.** Directional dissolution of a Zn@CS@Al<sub>2</sub>O<sub>3</sub> anode filament. (a) Schematics showing the directional dissolution mechanism of a Zn@CS@Al<sub>2</sub>O<sub>3</sub> anode filament in 0.9% NaCl solution. (yellow: Al<sub>2</sub>O<sub>3</sub>, green: CS, and black: Zn). (b) Discharge curve of a 5 mm Zn@CS@Al<sub>2</sub>O<sub>3</sub> filament at 0.01 mA. Optical image insets marked at different time points (24, 48, and 72 h) give the corresponding filament morphology (scale bars are 1 mm). (c–e) Representative SEM images of the Zn@CS@Al<sub>2</sub>O<sub>3</sub> filament obtained from different cross-sectional areas (i,ii) when the filament was discharged at different time points (c: 24, d: 48, and e: 72 h) as marked in panel (b). Images on the right are enlarged SEM pictures showing the morphology of a Zn MP. (Scale bars are 1 μm). (f) XRD characterizations of the Zn@CS@Al<sub>2</sub>O<sub>3</sub> filament at regions (i) and(ii) at different time points (24, 48, and 72 h).

based on the Zn oxidation reaction in saline solution (0.9% NaCl). Before the test, the front end of the fully packaged filament was cut off to expose Zn MPs inside. As schematically illustrated in Figure 2a, when the electrode filament was immersed in the electrolyte, Zn metal MPs at the exposed dissolution front would form a galvanic cell and react with OH<sup>−</sup> from the aqueous solution to form the initial byproduct of Zn(OH)<sub>2</sub>. The main body of the composite electrode was protected by Al<sub>2</sub>O<sub>3</sub> ALD coating. The protected Zn MP network formed a conductive channel, causing electrons to transport to the external load. The Zn(OH)<sub>2</sub> byproducts might loosely accumulate near the dissolution front region, which would eventually dissolve in biofluids. Following the dissolution of Zn MPs, the unsupported Al<sub>2</sub>O<sub>3</sub> thin sheets could easily come off and expose more Zn MP surfaces to sustain the continuous oxidation reaction. As such, the Zn MP network reacted and dissolved in sequence providing a constant supply of electric current within a finite period of time determined by the reaction rate and length of the composite anode filament. The effect of Al<sub>2</sub>O<sub>3</sub> coating was proved by comparing the discharging performances of 3 mm anode filaments with and without Al<sub>2</sub>O<sub>3</sub> coating. The filament without coating showed a rapid voltage drop to zero in 7 h compared to ~40 h stable discharging lifetime of the coated filament (Figure S3).

The operation of a Zn@CS@Al<sub>2</sub>O<sub>3</sub> anode filament was tested in saline (0.9% NaCl) solution and paired with an Aupolycaprolactone (PCL) cathode shown in Figure S4. At first, the electrical conductivity of the Zn@CS@Al<sub>2</sub>O<sub>3</sub> filament was evaluated by electrochemical impedance spectroscopy (EIS) (Figure S5). From the intercept of the real axis, the equivalent series resistance of Zn@CS@Al<sub>2</sub>O<sub>3</sub> was found to be ~120 Ω, suggesting that the composite filament was able to function as an electrode appropriately. The anode filaments with 5 mm length were then discharged at a current of 0.01 mA. The

discharge curve is shown in Figure 2b. A single filament exhibited an initial open-circuit voltage (V<sub>OC</sub>) of 0.83 V. This voltage was about half of the theoretical value (1.62 V) determined by the redox potential of Zn/Zn(OH)<sub>2</sub> (−1.22 V) and O<sub>2</sub>/OH<sup>−</sup> (0.40 V). This discrepancy could be attributed to the electrochemical overpotential required by the oxygen reduction to shift the O<sub>2</sub>/OH<sup>−</sup> half cell potential negatively because of slow electrochemical catalytic kinetics on Au surfaces, which has also been observed in Mg-based degradable batteries.<sup>17</sup> Upon discharging, the cell voltage quickly dropped and approached a relatively flat discharging plateau of ~0.5 V. The output voltage dropped to zero after ~84 h (3.5 days), indicating the end of battery life. Integration of the discharge profile revealed a total energy output of 1.57 J. Since a 5 mm filament contained ~3.5 mg of Zn MPs, theoretically, it could offer a specific capacity of 240 mA h g<sup>−1</sup>. The utilization rate was calculated by dividing the discharged Zn by the total mass of Zn MPs in the filament. A Zn@CS@Al<sub>2</sub>O<sub>3</sub>–Au–PCL battery achieved ~30% utilization rate in the 0.9% neutral NaCl saline solution, which was higher than most reported Mg-based bioresorbable batteries. Comparison of reported bioresorbable batteries regarding their output voltage and utilization rate is summarized in Table S1.

The directional dissolution of the Zn MP filament was examined by optical imaging. Insets in Figure 2b show the filament morphology change as the discharge progresses at different time points (24, 48, and 72 h). During this process, the dissolution front gradually converted into a white layer, and eventually, the entire filament was changed to white discharging products. A series of cross-sectional SEM images and corresponding XRD patterns were captured to illustrate time-dependent material and structural changes during the discharge process. SEM images are shown in Figure 2c–e, respectively, where regions (i) and (ii) represent the dissolution front and rear positions on the filament for cross-

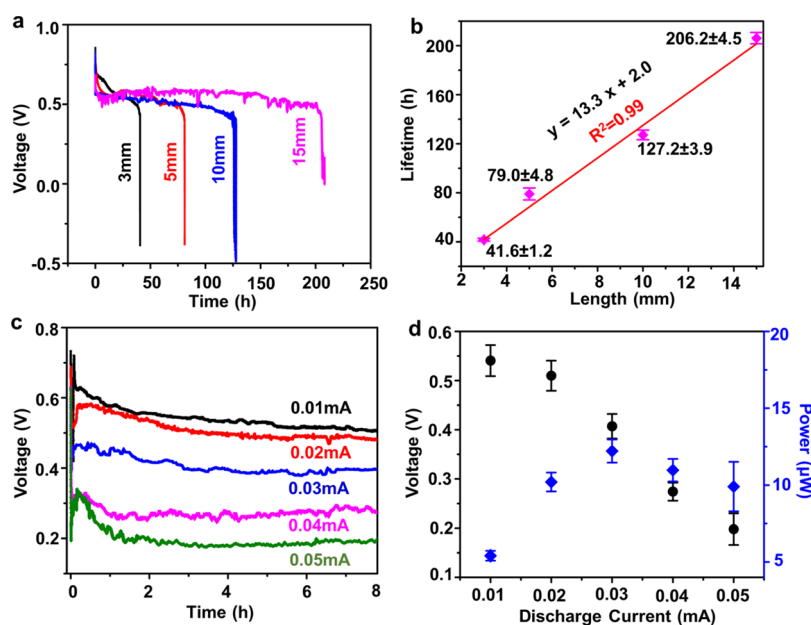


**Figure 3.** Controllable discharge lifetime and electric output of a single filament. (a) Galvanostatic discharge of single Zn@CS@Al<sub>2</sub>O<sub>3</sub> filaments with different lengths (3, 5, 10, and 15 mm) and the same cross-sectional area (2 × 0.17 mm<sup>2</sup>). Discharge current was fixed at 0.01 mA. (b) Single-cell lifetime extrapolated from panel (a) as a function of the filament length. A linear relationship was obtained ( $R^2 = 99\%$ , data are expressed as average ± SD,  $n = 3$ ). (c) Discharge characteristics of single Zn@CS@Al<sub>2</sub>O<sub>3</sub> filaments (5 × 2 × 0.17 mm<sup>3</sup>) at different discharge currents. (d) Stable plateau voltage obtained from panel (c) and calculated power as a function of discharge current. [Data are expressed as average ± SD ( $n = 3$ )].

sectional sample collection. At the early stage (24 h), the MPs at the dissolution front exhibited roughened surfaces with many small pores (Figure 2c-i), suggesting that the Zn MPs started dissolving in the electrolyte. The Zn MPs in the rear region remained intact with smooth surfaces (Figure 2c-ii). With discharging further to 48 h, Zn MPs at the front were intensively dissolved and turned into a sheet-like network structure (Figure 2d-i), while MPs in the rear region started to show signs of dissolution similar to those in Figure 2c-i. At 72 h, as the discharge nearly completed, both regions exhibited a similar porous morphology, indicating intensive dissolution (Figure 2e). This observation revealed that the dissolution of the composite filament followed the length direction and demonstrated a sequential reaction path as predicted.

XRD spectra were collected from both regions at these discharging time points to reveal the corresponding phase evolution (Figure 2f). At 24 h, both regions were still dominated by Zn (PDF#04-0831), while a small amount of zincite (ZnO) (PDF#36-1451)/Zn(OH)<sub>2</sub> (PDF#48-1066) appeared in the dissolution front (region i), indicated by the small peak at  $2\theta = 47.6$  and  $57.6^\circ$ . The ZnO/Zn(OH)<sub>2</sub> peaks started to show in the rear region at 48 h. More diffraction peaks appeared at the dissolution front, which could be indexed to simonkolleite (Zn<sub>5</sub>(OH)<sub>8</sub>Cl<sub>2</sub>·H<sub>2</sub>O) (PDF#07-0155). Near the end of discharge (72 h), both front and rear regions exhibited the same phase peak combinations. The end product was mostly composed of ZnO/Zn(OH)<sub>2</sub> with an appreciable portion of (Zn<sub>5</sub>(OH)<sub>8</sub>Cl<sub>2</sub>·H<sub>2</sub>O) (Figure S6). While Zn(OH)<sub>2</sub> was considered as the initial product during discharge, it tended to form more thermodynamically stable ZnO when more hydroxy ions were presented from the cathode oxygen reduction reaction.<sup>17,26</sup> In addition, with the presence of Cl<sup>-</sup> ions in the electrolyte, Zn(OH)<sub>2</sub> could react with Cl<sup>-</sup> forming simonkolleite and releasing OH<sup>-</sup>.<sup>27,28</sup> Therefore, biocompatible and bioresorbable ZnO/Zn(OH)<sub>2</sub>

and Zn<sub>5</sub>(OH)<sub>8</sub>Cl<sub>2</sub>·H<sub>2</sub>O were believed to be the main compounds constructing the remaining sheet-like network after discharge.<sup>29</sup> XPS survey spectra further confirmed the chemical states of the remaining compounds (Figure S7). The Zn 2p<sub>3/2</sub> peak could be deconvoluted into two characteristic peaks associated with ZnO/Zn(OH)<sub>2</sub> (1022.40 eV) and Zn<sub>5</sub>(OH)<sub>8</sub>Cl<sub>2</sub>·H<sub>2</sub>O (1021.71 eV).<sup>28</sup> The Cl 2p peak could also be deconvoluted into the Zn–Cl bond from Zn<sub>5</sub>(OH)<sub>8</sub>Cl<sub>2</sub>·H<sub>2</sub>O (198.64 eV) and NaCl residuals (200.4 eV).<sup>30</sup> Meanwhile, no Al peaks could be observed from the XPS spectrum of the residual compound, suggesting that this biocompatible Al<sub>2</sub>O<sub>3</sub> nano-film shell was peeled off from the composite during the dissolution process. Continuous zinc dissolution can raise the local pH slightly to further dissolve simonkolleite and zinc oxide into a soluble zinc salt over long-term degradation.<sup>31,32</sup>

To show the controllability of battery lifetime, Zn@CS@Al<sub>2</sub>O<sub>3</sub> anode filaments were made in different lengths and tested under the same conditions. As shown in Figure 3a, at a discharge current of 0.01 mA, all the filaments exhibited a close initial  $V_{OC}$  in the range of 0.83–0.95 V. The period of stable voltage span showed a clear correlation with the length of anode filaments. The 15 mm filament exhibited more than 200 h of lifetime (8.6 days), which was superior to most reported magnesium-based bioresorbable batteries shown in Table S1. Quantitative analysis revealed an almost linear relationship between the filament length and the discharge lifetime (Figure 3b), where each data point was obtained from three filament samples showing good reproducibility. The corresponding discharging curves and data were included in Figure S8 and Table S2, respectively. This decent linearity ( $R = 99\%$ ) further suggested that the Zn MPs in the composite were electrically and coherently connected and uniformly distributed. Therefore, the lifespan of this composite battery filament could be

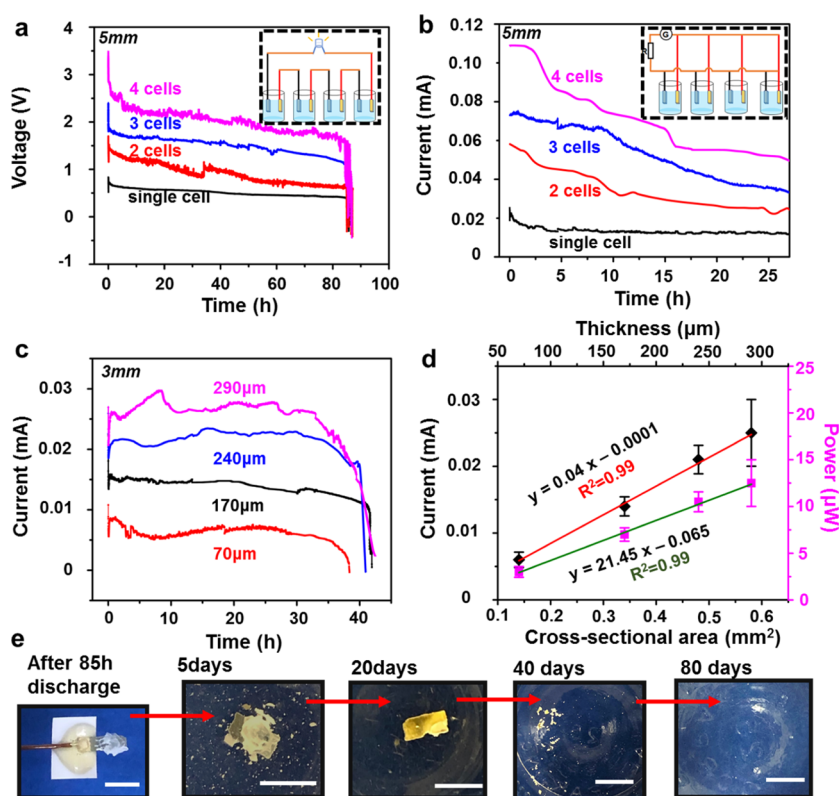


**Figure 4.** Filament integration performance and biodegradation behavior. (a) Galvanostatic discharge of multiple Zn@CS@Al<sub>2</sub>O<sub>3</sub> filaments when connected in series at a discharge current of 0.01 mA. All the filaments were 5 mm in length and had the same cross-sectional area of 0.17 × 2 mm<sup>2</sup>. The inset is the schematic of the connection setup. (b) Constant-voltage discharging curves of multiple Zn@CS@Al<sub>2</sub>O<sub>3</sub> filaments connected in parallel at a discharge voltage of 0.5 V. All the filaments were 5 mm in length and had the same cross-sectional area of 0.17 × 2 mm<sup>2</sup>. The inset is the schematic of connection setup. (c) Constant-voltage discharging profiles of a Zn@CS@Al<sub>2</sub>O<sub>3</sub> filament with different cross-sectional areas at a discharge voltage of 0.5 V. All the filaments had the same length of 3 mm and width of 2 mm with different thicknesses (70, 170, 240, and 290 μm). (d) Current output extrapolated from panel (c) and calculated power output plotted as a functional of the filament cross-sectional area showing a good linear relationship ( $R^2 = 99\%$ , data are expressed as average  $\pm$  SD,  $n = 3$ ). (e) Optical images showing the dissolution processes of the completely discharged Zn@CS@Al<sub>2</sub>O<sub>3</sub> filament in 0.9% NaCl solution. (Inset: scale bars are 5 mm).

customized according to application needs simply by varying the length.

The discharge behavior at different currents was further evaluated from the 5 mm composite filaments to investigate the output power of the battery. As shown in Figure 3c, when the discharge current was raised to 0.02 mA, the output voltage only slightly dropped to  $\sim 0.5$  V. However, as the discharging current further increased to 0.03 mA and above, the output voltage quickly dropped by  $\sim 0.08$  V per 0.01 mA current increment, which could commonly be attributed to the higher IR drop due to the finite battery internal resistance. From the result obtained from three filament samples at each discharging current, the statistic relationship between the output voltage and discharge current is plotted in Figure 3d. The output power was calculated by averaging discharge data from the first 8 h. At the discharge current of 0.03 mA, single-composite filaments reached a maximum power of 12 μW, which was adequate for small implantable medical electronics such as a sensing platform.<sup>33–37</sup>

To demonstrate the capability of integration, multiple Zn@CS@Al<sub>2</sub>O<sub>3</sub> degradable electrode filaments were connected in parallel and in series, and their discharging behavior was tested in a 0.9% NaCl electrolyte. First, two to four 5 mm-long filaments were connected in series and discharged at a constant current of 0.01 mA. As shown in Figure 4a, the output voltage plateau exhibited a monotonic increase as the number of

filaments increased. As the single filament had an output voltage of 0.55 V, two to four filaments gave output voltages of  $1.05 \pm 0.15$ ,  $1.6 \pm 0.2$ , and  $2.0 \pm 0.1$  V, where each filament made a nearly equal contribution of  $\sim 0.5$  V. All combinations exhibited the same lifetime of  $\sim 80$  h. The more obvious degradation of the voltage plateau compared to a single filament could be attributed to the increase in battery internal resistance primarily from the electrical connections among individual filaments. Five filaments connected in series could light up a red LED with 2.0 V threshold voltage for more than 40 h without any obvious intensity decay (Figure S9). Similarly, the discharge current could be improved by connecting multiple filaments in parallel. At a constant output voltage of 0.5 V, the discharge current increased as the number of filaments increased (Figure 4b). However, several abrupt drops in the current–time curve could also be observed, which was possibly due to the large non-uniformity in individual filament performance. In this regard, a more reliable way to improve the discharge current could be to increase the cross-sectional area of a single filament. A series of 3 mm filaments were fabricated with a thickness of 70 μm, 170, 240, and 290 μm at the same width of 2 mm (Figure S10) and were discharged at a constant voltage of 0.5 V. As shown in Figure 4c, the output currents exhibited a proportional relationship with the filament thickness or cross-sectional area. The stable output current increased from  $0.006 \pm 0.001$  mA of the 70 μm

filament to  $0.014 \pm 0.001$ ,  $0.021 \pm 0.002$ , and  $0.025 \pm 0.005$  mA for 170, 240, and 290  $\mu\text{m}$ -thick filaments, respectively (Figure 4d). This good linear relationship ( $R^2 = 99\%$ ) suggested that the output current from the composite filaments was nearly  $0.043 \text{ mA mm}^{-2}$ . It should be noted that the relatively small cross-sectional area used in this study was due to the high requirement of homogeneity of Zn MPs in the filaments. In principle, the output current can be scaled to the mA level by further increasing the filament cross-sectional area with the help of more advanced manufacturing techniques.

Directional degradation in biological fluids while providing controllable electricity output demonstrated a promising potential for the application of a transient implantable DC power source. As revealed in the structure characterization, the degradation would primarily yield ZnO-based byproducts, which could further dissolve completely in the biological environment. In order to show this principle, the dissolution process of a completely discharged Zn@CS@Al<sub>2</sub>O<sub>3</sub> anode filament was investigated in 0.9% NaCl saline solution. The saline solution was refreshed every day to mimic the physiological environment. As shown in Figure 4e, the discharged filament could be completely dissolved in the saline solution over an extended period of time, indicating a good potential as an *in vivo* bioresorbable power source. It should be noted that this work only focused on the anode. The cathode was made with Au-PCL, which was also biocompatible, and PCL can degrade slowly in a biological environment over months to years.<sup>19,38</sup> To form a completely bioresorbable transient battery, the biodegradability of the cathode should also be investigated and controlled within the same time scale. This, although another essential perspective of the battery development, is beyond the scope of this work.

### 3. CONCLUSIONS

In summary, we developed a degradable Zn primary battery anode based on a Zn MPs@chitosan@Al<sub>2</sub>O<sub>3</sub> core–double-shell composite structure. When interfacing with biofluids, the Zn MPs would start to dissolve, forming a primary battery system. ALD Al<sub>2</sub>O<sub>3</sub> coating ensured the sequential dissolution of Zn MPs and thus controlled the lifetime and output. A single-composite anode filament showed stable 0.55 V output voltage at a discharging current of 0.01 mA. The discharging time was linearly related to the length of the filament. For a 5 mm-long filament, it was able to produce 80 h of stable DC electricity, which could be extended to more than 200 h by increasing the length to 15 mm. Varying the discharging current revealed that the maximum output power was  $\sim 12 \mu\text{W}$  at 0.03 mA, which was adequate for powering small implantable electronics. Integrating the filaments in series could effectively raise the output voltage at the same discharging current, allowing successful operation of small electronics with operation voltage higher than that could be provided by an individual filament. By increasing the filament cross-sectional area, higher current output could be achieved at the same discharging voltage, raising the output power. The final discharging byproducts, mostly ZnO/Zn(OH)<sub>2</sub>, could slowly dissolve in biofluids, making this composite filament completely degradable. This development demonstrated a promising solution for enabling a bioresorbable battery system to power transient implantable electronics with tunable power output and lifetime.

## 4. EXPERIMENTAL SECTION

**4.1. Zn@Chitosan@Al<sub>2</sub>O<sub>3</sub> Anode Processing.** A suspension composed of 300 mg of Zn MPs ( $<10 \mu\text{m}$ , Sigma) and IPA ( $\geq 99.5\%$ , Sigma) solvent with a ratio of Zn: IPA = 1:3 by weight was stirred for 10 min and then poured into a plasma desorption mass spectrometry (PDMS) mold with a groove area of  $6 \times 1 \text{ cm}^2$ . After 2 min of sedimentation, 10% acetic acid ( $\geq 99.0\%$ , Sigma) was dropped into the Zn groove area and let to sit for 30 min in atmosphere and room temperature for electrochemical sintering.<sup>39</sup> A total of 2 wt % chitosan/acetic acid solution was prepared by adding 0.4 g of chitosan (85% DD, Fisher Scientific) into 20 mL of 1% acetic acid with 4 h of stirring. A total of 0.5 mL of this solution was dropped into the groove, followed by air drying in atmosphere. The Zn@chitosan composite film was peeled off from the PDMS mold and cut into filaments with designated length and width. Home-made ALD was utilized to grow amorphous Al<sub>2</sub>O<sub>3</sub> on the Zn@chitosan filaments. Al<sub>2</sub>O<sub>3</sub> ALD was conducted at 90 °C using trimethylaluminum (TMA) and H<sub>2</sub>O as precursors. The pulsing time for TMA and H<sub>2</sub>O was both 0.5 s and separated by 30 s N<sub>2</sub> purging. A total of 200 cycles of ALD were implemented to grow 20 nm amorphous Al<sub>2</sub>O<sub>3</sub> thin films.

**4.2. Au-PCL Cathode Fabrication.** A total of 1 g of PCL (PCL,  $M_w \approx 70,000$ , Fisher Scientific) fillers were dissolve into 10 mL of acetone and then cast into a glass Petri dish to be dried for 4 h in water vapor heat to prepare the PCL bioresorbable polymer film ( $\sim 20 \mu\text{m}$ ). A thin-film cathode consisting of 50 nm of gold was deposited by sputtering (Leica EM ACE600) onto the PCL film.

**4.3. Battery Assembly and Discharge Test.** A Zn@chitosan@Al<sub>2</sub>O<sub>3</sub> anode and Au-PCL film cathode were connected through a Cu wire affixed with silver paste (EPO-TEK H20E). After being dried in hood, the connection areas between the electrode and wire were encapsulated with epoxy. Before the test, the front end of the Zn@chitosan@Al<sub>2</sub>O<sub>3</sub> anode filament was cut off to expose Zn MPs inside. Both electrodes were immersed into 0.9% NaCl ( $\geq 99.0\%$ , Sigma) saline to assemble a primary battery under room temperature. The discharge behavior was tested on a multichannel battery testing system (LAND CT2001A) at different discharge currents. EIS was conducted on an Autolab potentiostat/galvanostat (PGSTAT302N). The EIS frequency range was from 0.1 to 10,000 Hz under open-circuit conditions. Ag/AgCl ( $\geq 99.0\%$ , 3 M KCl) and Pt wire were used as the reference and counter electrodes, respectively. Based on the discharge test, the total energy output  $W(\text{J})$  and the specific capacity  $C_s (\text{mA h g}^{-1})$  were calculated by eqs 1 and 2, where  $m$ ,  $I$ ,  $t$ , and  $V_{\text{av}}$  refer to the mass (g), discharge current (mA), discharge time (h), and average discharge potential (V) of the cells, respectively.

$$W = V_{\text{av}} \times I \times t \quad (1)$$

$$C_s = \frac{I \times t}{m} \quad (2)$$

**4.4. Structure and Morphology Characterization.** SEM and EDS observations were performed on a Zeiss LEO 1530 field-emission microscope. XRD patterns were obtained on the Bruker D8 Discovery with Cu K $\alpha$  radiation. The XPS spectrum was acquired using a Thermo Scientific K-alpha XPS instrument.

**4.5. Battery Anode Biodegradation.** The anode dissolution experiment was carried out under 85 °C in 0.9% NaCl saline in an oven. A total of 0.9% NaCl saline solution was removed completely using a syringe every 24 h, and then, the container was refilled by adding fresh NaCl saline. An optical image was taken to trace the anode degradation process.

**4.6. Statistical Analysis.** The data were taken from at least three independent experiments, and all obtained data were expressed as average  $\pm$  standard deviation (SD).

## ■ ASSOCIATED CONTENT

### Supporting Information

The Supporting Information is available free of charge at <https://pubs.acs.org/doi/10.1021/acsami.1c00602>.

Scanning electronic microscopy image; EDS elemental mapping; EIS Nyquist plot; performance comparison among bioresorbable batteries; detailed XRD and XPS analysis; reproducibility of discharging lifetime related with filament length; and photo of the battery in series lighting a LED (PDF)

## AUTHOR INFORMATION

### Corresponding Author

**Xudong Wang** – Department of Materials Science and Engineering, University of Wisconsin–Madison, Madison, Wisconsin 53706, United States; [orcid.org/0000-0002-9762-6792](https://orcid.org/0000-0002-9762-6792); Email: [xudong.wang@wisc.edu](mailto:xudong.wang@wisc.edu)

### Authors

**Yutao Dong** – Department of Materials Science and Engineering, University of Wisconsin–Madison, Madison, Wisconsin 53706, United States; [orcid.org/0000-0003-3582-087X](https://orcid.org/0000-0003-3582-087X)

**Jun Li** – Department of Materials Science and Engineering, University of Wisconsin–Madison, Madison, Wisconsin 53706, United States; [orcid.org/0000-0002-7498-6736](https://orcid.org/0000-0002-7498-6736)

**Fan Yang** – Department of Materials Science and Engineering, University of Wisconsin–Madison, Madison, Wisconsin 53706, United States

**Yizhan Wang** – Department of Materials Science and Engineering, University of Wisconsin–Madison, Madison, Wisconsin 53706, United States; [orcid.org/0000-0003-0464-6610](https://orcid.org/0000-0003-0464-6610)

**Ziyi Zhang** – Department of Materials Science and Engineering, University of Wisconsin–Madison, Madison, Wisconsin 53706, United States; [orcid.org/0000-0001-9102-8292](https://orcid.org/0000-0001-9102-8292)

**Jingyu Wang** – Department of Materials Science and Engineering, University of Wisconsin–Madison, Madison, Wisconsin 53706, United States

**Yin Long** – Department of Materials Science and Engineering, University of Wisconsin–Madison, Madison, Wisconsin 53706, United States; [orcid.org/0000-0002-6602-0210](https://orcid.org/0000-0002-6602-0210)

Complete contact information is available at:  
<https://pubs.acs.org/10.1021/acsami.1c00602>

### Notes

The authors declare no competing financial interest.

## ACKNOWLEDGMENTS

The research is primarily supported by the U.S. Department of Energy (DOE), Office of Science, Basic Energy Sciences (BES), under award # DE-SC0020283.

## REFERENCES

- (1) Zvezdin, A.; Di Mauro, E.; Rho, D.; Santato, C.; Khalil, M. E. Route toward Sustainable Organic Electronics. *MRS Energy Sustain.* **2020**, *7*, No. E16.
- (2) Irimia-Vladu, M.; Troshin, P. A.; Reisinger, M.; Shmygleva, L.; Kanbur, Y.; Schwabegger, G.; Bodea, M.; Schwödiauer, R.; Mumyatov, A.; Fergus, J. W.; Razumov, V. F.; Sitter, H.; Sariciftci, N. S.; Bauer, S. Biocompatible and Biodegradable Materials for Organic Field-Effect Transistors. *Adv. Funct. Mater.* **2010**, *20*, 4069–4076.
- (3) Kim, D.-H.; Viventi, J.; Amsden, J. J.; Xiao, J.; Vigeland, L.; Kim, Y.-S.; Blanco, J. A.; Panilaitis, B.; Frechette, E. S.; Contreras, D.; Kaplan, D. L.; Omenetto, F. G.; Huang, Y.; Hwang, K.-C.; Zakin, M.

- R.; Litt, B.; Rogers, J. A. Dissolvable Films of Silk Fibroin for Ultrathin Conformal Bio-integrated Electronics. *Nat. Mater.* **2010**, *9*, 511–517.
- (4) Hwang, S.-W.; Park, G.; Cheng, H.; Song, J.-K.; Kang, S.-K.; Yin, L.; Kim, J.-H.; Omenetto, F. G.; Huang, Y.; Lee, K.-M.; Rogers, J. A. Semiconductors: 25th Anniversary Article: Materials for High-Performance Biodegradable Semiconductor Devices. *Adv. Mater.* **2014**, *26*, 1949.
- (5) Fu, K. K.; Wang, Z.; Dai, J.; Carter, M.; Hu, L. Transient Electronics: Materials and Devices. *Chem. Mater.* **2016**, *28*, 3527–3539.
- (6) Li, R.; Wang, L.; Yin, L. Materials and Devices for Biodegradable and Soft Biomedical Electronics. *Materials* **2018**, *11*, 2108.
- (7) Chae, J. S.; Park, S. K.; Roh, K. C.; Park, H. S. Electrode Materials for Biomedical Patchable and Implantable Energy Storage Devices. *Energy Storage Mater.* **2020**, *24*, 113–128.
- (8) Jia, X.; Wang, C.; Lee, C.-Y.; Yu, C.; Wallace, G. G. Energy Materials for Transient Power Sources. *MRS Bull.* **2020**, *45*, 121–128.
- (9) Hwang, S.-W.; Tao, H.; Kim, D.-H.; Cheng, H.; Song, J.-K.; Rill, E.; Brenckle, M. A.; Panilaitis, B.; Won, S. M.; Kim, Y.-S.; Song, Y. M.; Yu, K. J.; Ameen, A.; Li, R.; Su, Y.; Yang, M.; Kaplan, D. L.; Zakin, M. R.; Slepian, M. J.; Huang, Y.; Omenetto, F. G.; Rogers, J. A. A Physically Transient Form of Silicon Electronics. *Science* **2012**, *337*, 1640–1644.
- (10) Dagdeviren, C.; Hwang, S.-W.; Su, Y.; Kim, S.; Cheng, H.; Gur, O.; Haney, R.; Omenetto, F. G.; Huang, Y.; Rogers, J. A. Transient, Biocompatible Electronics and Energy Harvesters Based on ZnO. *Small* **2013**, *9*, 3398–3404.
- (11) Jiang, W.; Li, H.; Liu, Z.; Li, Z.; Tian, J.; Shi, B.; Zou, Y.; Ouyang, H.; Zhao, C.; Zhao, L.; Sun, R.; Zheng, H.; Fan, Y.; Wang, Z. L.; Li, Z. Fully Bioabsorbable Natural-Materials-Based Triboelectric Nanogenerators. *Adv. Mater.* **2018**, *30*, 1801895.
- (12) Wang, X.; Xu, W.; Chatterjee, P.; Lv, C.; Popovich, J.; Song, Z.; Dai, L.; Kalani, M. Y. S.; Haydel, S. E.; Jiang, H. Food-Materials-Based Edible Supercapacitors. *Adv. Mater. Technol.* **2016**, *1*, 1600059.
- (13) Lee, G.; Kang, S.-K.; Won, S. M.; Gutruf, P.; Jeong, Y. R.; Koo, J.; Lee, S.-S.; Rogers, J. A.; Ha, J. S. Fully Biodegradable Microsupercapacitor for Power Storage in Transient Electronics. *Adv. Energy Mater.* **2017**, *7*, 1700157.
- (14) Lee, H.; Lee, G.; Yun, J.; Keum, K.; Hong, S. Y.; Song, C.; Kim, J. W.; Lee, J. H.; Oh, S. Y.; Kim, D. S.; Kim, M. S.; Ha, J. S. Facile Fabrication of a Fully Biodegradable and Stretchable Serpentine-Shaped Wire Supercapacitor. *Chem. Eng. J.* **2019**, *366*, 62–71.
- (15) Yin, L.; Cheng, H.; Mao, S.; Haasch, R.; Liu, Y.; Xie, X.; Hwang, S.-W.; Jain, H.; Kang, S.-K.; Su, Y.; Li, R.; Huang, Y.; Rogers, J. A. Dissolvable Metals for Transient Electronics. *Adv. Funct. Mater.* **2014**, *24*, 645–658.
- (16) Huang, X.; Wang, D.; Yuan, Z.; Xie, W.; Wu, Y.; Li, R.; Zhao, Y.; Luo, D.; Cen, L.; Chen, B.; Wu, H.; Xu, H.; Sheng, X.; Zhang, M.; Zhao, L.; Yin, L. A Fully Biodegradable Battery for Self-Powered Transient Implants. *Small* **2018**, *14*, 1800994.
- (17) Jia, X.; Wang, C.; Ranganathan, V.; Napier, B.; Yu, C.; Chao, Y.; Forsyth, M.; Omenetto, F. G.; MacFarlane, D. R.; Wallace, G. G. A Biodegradable Thin-Film Magnesium Primary Battery Using Silk Fibroin-Ionic Liquid Polymer Electrolyte. *ACS Energy Lett.* **2017**, *2*, 831–836.
- (18) Yin, L.; Huang, X.; Xu, H.; Zhang, Y.; Lam, J.; Cheng, J.; Rogers, J. A. Materials, Designs, and Operational Characteristics for Fully Biodegradable Primary Batteries. *Adv. Mater.* **2014**, *26*, 3879–3884.
- (19) Tsang, M.; Armutlulu, A.; Martinez, A. W.; Allen, S. A. B.; Allen, M. G. Biodegradable Magnesium/Iron Batteries With Polycaprolactone Encapsulation: A Microfabricated Power Source for Transient Implantable Devices. *Microsyst. Nanoeng.* **2015**, *1*, 15024.
- (20) Jia, X.; Wang, C.; Zhao, C.; Ge, Y.; Wallace, G. G. Toward Biodegradable Mg-Air Bioelectric Batteries Composed of Silk Fibroin-Polypyrrole Film. *Adv. Funct. Mater.* **2016**, *26*, 1454–1462.
- (21) Wang, J.; Tang, J.; Zhang, P.; Li, Y.; Wang, J.; Lai, Y.; Qin, L. Surface Modification of Magnesium Alloys Developed for Bioabsorb-

able Orthopedic Implants: A General Review. *J. Biomed. Mater. Res., Part B* **2012**, *100B*, 1691–1701.

(22) Peng, F.; Li, H.; Wang, D.; Tian, P.; Tian, Y.; Yuan, G.; Xu, D.; Liu, X. Enhanced Corrosion Resistance and Biocompatibility of Magnesium Alloy by Mg-Al-Layered Double Hydroxide. *ACS Appl. Mater. Interfaces* **2016**, *8*, 35033–35044.

(23) Vojtěch, D.; Kubasek, J.; Capek, J.; Pospisilova, I. Comparative Mechanical and Corrosion Studies on Magnesium, Zinc, and Iron Alloys as Biodegradable Metals. *Mater. Technol.* **2015**, *49*, 877–882.

(24) Nadeau, P.; El-Damak, D.; Glettig, D.; Kong, Y. L.; Mo, S.; Cleveland, C.; Booth, L.; Roxhed, N.; Langer, R.; Chandrakasan, A. P.; Traverso, G. Prolonged Energy Harvesting for Ingestible Devices. *Nat. Biomed. Eng.* **2017**, *1*, 0022–0028.

(25) Peng, H.; Wang, K.; Huang, Z. An Injection Molding Method to Prepare Chitosan-Zinc Composite Material for Novel Biodegradable Flexible Implant Devices. *Mater. Manuf. Processes* **2019**, *34*, 256–261.

(26) Wang, B. Recent Development of Non-Platinum Catalysts for Oxygen Reduction Reaction. *J. Power Sources* **2005**, *152*, 1–15.

(27) Falk, T.; Svensson, J. E.; Johansson, L. G. The Influence of CO<sub>2</sub> and NaCl on the Atmospheric Corrosion of Zinc: A Laboratory Study. *J. Electrochem. Soc.* **1998**, *145*, 2993.

(28) Meng, Y.; Liu, L.; Zhang, D.; Dong, C.; Yan, Y.; Volinsky, A. A.; Wang, L.-N. Initial Formation of Corrosion Products on Pure Zinc in Saline Solution. *Bioact. Mater.* **2019**, *4*, 87–96.

(29) Tong, X.; Shi, Z.; Xu, L.; Lin, J.; Zhang, D.; Wang, K.; Li, Y.; Wen, C. Degradation behavior, cytotoxicity, hemolysis, and antibacterial properties of electro-deposited Zn-Cu metal foams as potential biodegradable bone implants. *Acta Biomater.* **2020**, *102*, 481–492.

(30) Winiarski, J.; Tylus, W.; Winiarska, K.; Szczygiel, I.; Szczygiel, B. XPS and FT-IR Characterization of Selected Synthetic Corrosion Products of Zinc Expected in Neutral Environment Containing Chloride Ions. *J. Spectrosc.* **2018**, *2018*, 2079278.

(31) Liu, X.; Yang, H.; Xiong, P.; Li, W.; Huang, H.-H.; Zheng, Y. Comparative Studies of Tris-HCl, HEPES and NaHCO<sub>3</sub>/CO<sub>2</sub> Buffer Systems on the Biodegradation Behavior of Pure Zn in NaCl and SBF Solutions. *Corros. Sci.* **2019**, *157*, 205–219.

(32) Kannan, M. B.; Moore, C.; Saptarshi, S.; Somasundaram, S.; Rahuma, M.; Lopata, A. L. Biocompatibility and Biodegradation Studies of A Commercial Zinc Alloy for Temporary Mini-implant Applications. *Sci. Rep.* **2017**, *7*, 15605.

(33) Tekeste, T.; Saleh, H.; Mohammad, B.; Ismail, M. Ultra-Low Power QRS Detection and ECG Compression Architecture for IoT Healthcare Devices. *IEEE Trans. Circuits and Syst. I: Regul. Pap.* **2019**, *66*, 669–679.

(34) Wang, Y.; Wang, Y.; Yang, Y. Graphene-Polymer Nanocomposite-Based Redox-Induced Electricity for Flexible Self-Powered Strain Sensors. *Adv. Energy Mater.* **2018**, *8*, 1800961.

(35) Wang, Y.; Yang, Y. Superhydrophobic Surfaces-Based Redox-Induced Electricity From Water Droplets For Self-Powered Wearable Electronics. *Nano Energy* **2019**, *56*, 547–554.

(36) Wang, Y.; Jiang, Y.; Wu, H.; Yang, Y. Floating Robotic Insects to Obtain Electric Energy from Water Surface for Realizing Some Self-Powered Functions. *Nano Energy* **2019**, *63*, 103810.

(37) Wu, H.; Xu, L.; Wang, Y.; Zhang, T.; Zhang, H.; Bowen, C. R.; Wang, Z. L.; Yang, Y. Enhanced Power Generation from the Interaction between Sweat and Electrodes for Human Health Monitoring. *ACS Energy Lett.* **2020**, *5*, 3708–3717.

(38) Zada, M. H.; Kumar, A.; Elmalak, O.; Markovitz, E.; Ickson, R.; Domb, A. J. In vitro and in vivo degradation behavior and the long-term performance of biodegradable PLCL balloon implants. *Int. J. Pharm.* **2020**, *574*, 118870.

(39) Lee, Y. K.; Kim, J.; Kim, Y.; Kwak, J. W.; Yoon, Y.; Rogers, J. A. Room Temperature Electrochemical Sintering of Zn Microparticles and Its Use in Printable Conducting Inks for Bioresorbable Electronics. *Adv. Mater.* **2017**, *29*, 1702665.